Biotechnology Notes 4 (2023) 150–159

Contents lists available at ScienceDirect

Biotechnology Notes

journal homepage: www.keaipublishing.com/en/journals/biotechnology-notes/

The electrical transport and antibacterial properties of Fe doped MgO nanoparticles synthesized by a soft chemical technique

Joyshree Maji [a,*], Sanjeev Pandey [c], Soumen Basu [b]

[a] Department of Physics, Asansol Engineering College, Asansol, West Bengal, 713304, India
[b] Department of Physics, National Institute of Technology Durgapur, West Bengal, 713209, India
[c] Department of Botany, Banwarilal Bhalotia College, Asansol, 713303, India

ARTICLE INFO

Keywords:
Fe doped MgO nanoparticles
Antibacterial effect
Electrical transport properties

ABSTRACT

Fe doped MgO nanoparticles were synthesized using a straightforward soft chemical method. We conducted a comprehensive examination of the electrical properties of Fe-doped MgO nanoparticles with a crystalline size range of 7–10 nm. Simultaneously, we explored their antibacterial capabilities. Our findings indicate that an increase in the concentration of Fe-doped MgO correlates with an enhanced bactericidal effect. To gain a deeper understanding of charge transfer processes, the AC conductivity and dielectric characteristics of the samples across various temperatures and frequencies was studied.The antibacterial activity was studied utilising the MIC methodology, the live count (LC) method, and the agar cup technique in addition to the electrical characteristics. After exposure to nanoparticles, we observed the disruption of pathogenic cell walls through transmission electron microscopy (TEM) analysis. These results suggest that Fe-doped MgO nanoparticles hold promise for the development of novel, more effective antibacterial drugs. The ½ MIC for *E.coli* was found to be 2.75 μg/ml, while for *Bacillus* sp., it was 1.75 μg/ml when exposed to Fe-doped MgO nanoparticles. This dosage level may find applications in the medical field. However, further investigations are required to assess potential toxicity and long-term environmental and human health effects. If successful in vivo tests follow, Fe-doped MgO nanoparticles could emerge as valuable antibacterial agents.

1. Introduction

Based on idea of science and its application nanotechnology deals with the teasing of matter at very small sizes (1–100 nm).[1] Its profound influence extends across multiple domains, including medicine, electronics, and energy, enabling the creation of novel materials with exceptional properties that were once deemed unattainable. In recent and upcoming research, nanomaterials have been shown to exhibit antibacterial activity. Contemporary technological strides in sample preparation and device fabrication are reflected in the physical characteristics of objects in today's world, occasionally leading to transformative discoveries.[2] However, the essence of this scientific exploration delves into the biological transformations that occur when certain elements are reduced to the nanoscale. A major concern within advanced nanoscience is the environmental impact of nanoparticles. A productive method for evaluating their non-toxicity involves examining bacterial reactions to these nanoparticles.[3] Incorporating nanoparticles into the realm of nanomedicine is a challenging task, primarily due to the stringent requirement that their dimensions align with those of biological systems. Given their inherent nanoscale size, nanomaterials stand as the most promising solution to address this requirement. Moreover, their unique physicochemical attributes render them exceptionally suitable for drug delivery, imaging, and sensing applications in the field of nanomedicine. These attributes include a high surface area-to-volume ratio and tunable surface chemistry. The diminutive size of nanoparticles is advantageous for medical innovations, as they are perceived to be less intrusive and, in some cases, biocompatible. Another benefit lies in the flexibility to fine-tune the physical and chemical properties of nanoparticles to cater to diverse applications, paving the way for the development of specialized nanomedicines.[4] Additionally, increased bio distribution of the medicine is demonstrated by medication delivery strategy.[5] Because of their potential antibacterial activity particularly with regard to combating antibiotic resistance, nanoparticles have also been assessed as nano-antibiotics in various situations.[6,7] In the realm of medical science, there has been a burgeoning interest in the prospective role of nanomaterials as cutting-edge

* Corresponding author.
E-mail address: nanoedutech@gmail.com (J. Maji).

https://doi.org/10.1016/j.biotno.2023.12.002
Received 21 October 2023; Received in revised form 1 December 2023; Accepted 5 December 2023
Available online 10 December 2023
2665-9069/© 2023 The Authors. Publishing services by Elsevier B.V. on behalf of KeAi Communications Co. Ltd. This is an open access article under the CC BY-NC-ND license (http://creativecommons.org/licenses/by-nc-nd/4.0/).

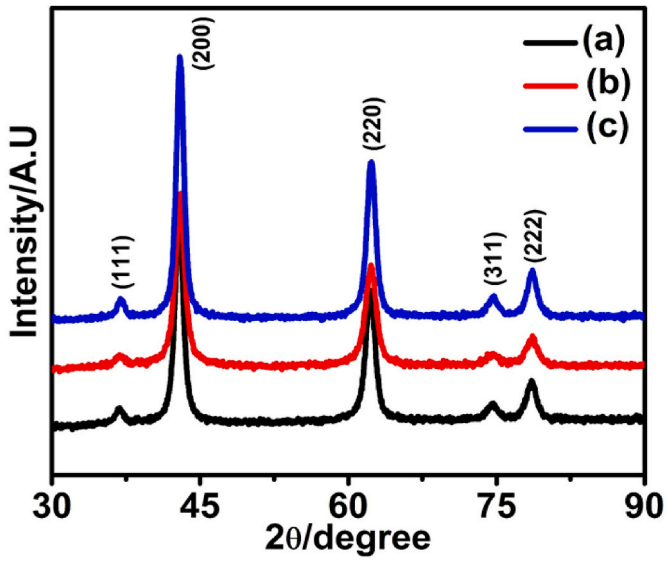

Fig. 1. (a–c) The diffraction pattern of X-Ray of 0.2 wt %, 0.6 wt% and 1.0 wt% Fe doped MgO nanoparticles respectively.

Table 1
Lattice Constant measurement.

Sample	Lattice constant a = b = c (A°)	Unit cell volume V = a^3 $(A°)^3$
0.2 wt% Fe doped MgO	4.2113	74.6876
0.6 wt% Fe doped MgO	4.1973	73.9452
1 wt% Fe doped MgO	4.2066	74.4378

solutions for cancer treatment.[8] Researchers have made significant strides in enhancing the performance of nanoparticles for in vivo imaging, resulting in the creation of nanoparticles with superior imaging capabilities.[9] Departing from conventional molecular fluorophores, there is a noteworthy development in the design of metallic nanoparticle-based fluorescent nanomaterials, which offer enhanced contrast for imaging purposes.[10,11] These metallic nanomaterials have demonstrated effectiveness in accurately identifying various vascular diseases.[12] Due to their electrical, magnetic, and antibacterial properties, metal oxide nanoparticles have also received a lot of interest recently. Additionally, the usage of metal oxide nanoparticles resulted in extremely positive antibacterial activity, allowing for the monitoring of bacterial infections that are frequently present following organ and tissue removal and replacement surgery.[13] Magnesium oxide (MgO) nanoparticle use in nanomedicine has recently attracted a lot of interest.[14] The Food and Drug Administration (FDA)[15] defines the MgO as a recognized as safe (GRAS) compound, which shows lot of applications in biomedical domain because it is a cheap and abundant substance. The different nanostructured MgO such as thin films,[16,17] nanowires (NWs),[18] flower-like structures[19] nanorods (NRs),[20] nanobelts,[21] and nanoparticles (NPs)[22] could be comfortably using routes such as sol-gel technique, hydrothermal routes, and vapour-phase deposition methods. In this article, the killing activity of Iron doped Magnesium oxide nanoparticles were discussed for the action of both *E.coli* and *Bacillus* sp.. The Fe doped MgO nanoparticles were synthesized by using a simple soft chemical technique. The synthesized materials have been characterized by using different state of art techniques. The substantial surface-to-volume ratio is widely recognized for its effectiveness in facilitating interactions at the interface between bacterial cell walls and materials. These interactions are likely responsible for enhancing antibacterial efficacy.

2. Materials and methods

2.1. Materials

Sodium hydroxide palate [NaOH] (MERCK, India), Magnesium Nitrate [$Mg(NO_3)_2,H_2O$] (MERCK, India), Ferric Nitrate [$Fe(NO_3)_3,H_2O$] (MERCK, India), Citrate acid [$C_6H_80_7$] (MERCK, India), and Ethylene glycol [$C_2H_6O_2$] (MERCK, India) were used as precursor materials. The materials have been used without any more purification. In this work two microbes *E.coli* and *Bacillus* sp. (Botany Department, B.B College, West Bengal,India) were used.

2.2. Synthesis of nanoparticle

Fe-doped MgO nanoparticles with different dopant concentrations were prepared by sol-gel route. For synthesize the above nanoparticles the appropriate molar ratios of Mg $(NO_3)_2,H_2O$ and $Fe(NO_3)_3,H_2O$ were combined in deionized water in the correct molar ratios to produce the first solution. Then, citrate acid ($C_6H_80_7$) and ethylene glycol ($C_2H_6O_2$) were added to the mixed solution and after that the solution was taken for heating at 90 °C to form the gel. The retrieved gel was first heated at 250 °C for 2.5 h and then calcined at 500 °C for 40 min. The crushed samples were subjected to annealing for different durations at a range of temperatures, including 2.5 h.

2.3. Characterization

2.3.1. Micro structural characterization

The X-ray diffraction pattern was used to confirm the crystalline arrangement of Fe doped MgO nanocrystals with different concentrations of Fe (0.2 wt%, 0.6 wt% & 1 wt%). X-ray diffraction pattern were obtained using an X-Pert Pro X-ray diffractometer (PANLYTICAL, Almelo, Netherlands) with nickel filtered Cu-K_α radiation of wavelength 1.54Å in the 2θ range from 20° to 80° to validate the crystalline of the various concentrations of dopant (Fe).

To examine the particle size and crystalline characteristics of the prepared sample, the Transmission Electron Microscopy (HRTEM, JEOL 2011) technique was employed. The nanoparticles were prepared by grinding and dispersing them in an ultrasonicator with ethanol, and measurements were taken using a 300-mesh carbon-coated copper grid. Furthermore, the morphology of the experimental pathogens was assessed using a 200 KV TEM (Transmission Electron Microscope) at the ½ MIC values of 2.5 μg/ml and 1.75 μg/ml. An untreated culture serves as a control in this experiment. The cultures were grown for 48 h and it was kept at 5000 rpm at room temperature. After being washed twice with 1X PBS (Phosphate Buffer Saline), the cultures were again washed with 100 % ethanol and kept in the same at a cell density of 10^8/ml for future use. Carbon –coated copper grid has been used for gridding the cultures at room temperature for analysis.

The value of dielectric constant and ac conductivity was calculated using an Agilent E4980A LCR metre over a frequency range of 20 Hz to 1 MHz within temperature from 313K to 473 K. The dielectric constant, $\varepsilon'(f)$ was derived by the given equation

$$\varepsilon'(f) = \frac{C_p t}{s\varepsilon_0}$$

Where t defines the thickness of testing disk and s is the area of surface of the above mentioned disk respectively.

2.3.2. Antibacterial assay study and determination of minimum inhibitory concentration (MIC)

Through the agar-cup method, 90 mm diameter Petri dishes were filled with 25 ml of nutrient-rich agar material. Subsequently, cups were created using a 9 mm cork-borer, and a bacterial lawn was cultivated using the 0.8 % top agar overlay technique. Fe doped MgO nanoparticle

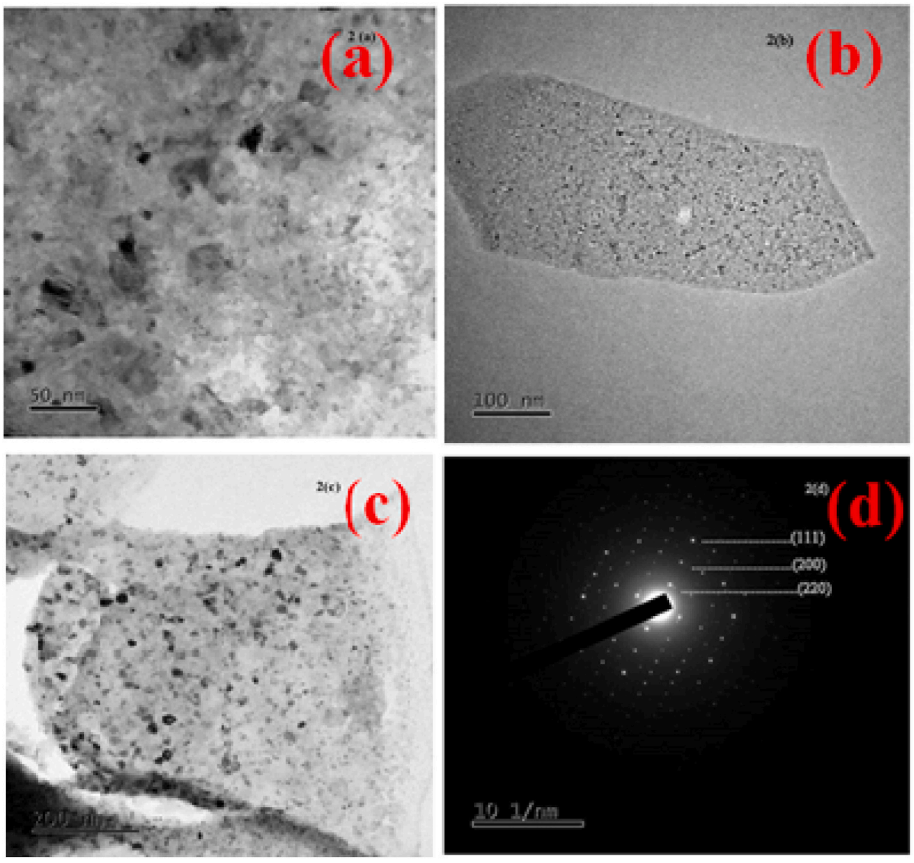

Fig. 2. (a–c) Transmission electron micrograph of 0.2 wt %, 0.6 wt% and 1.0 wt% Fe doped MgO nanoparticle respectively.Fig. 2 (d) SAD patterns of Fe doped MgO nanoparticles.

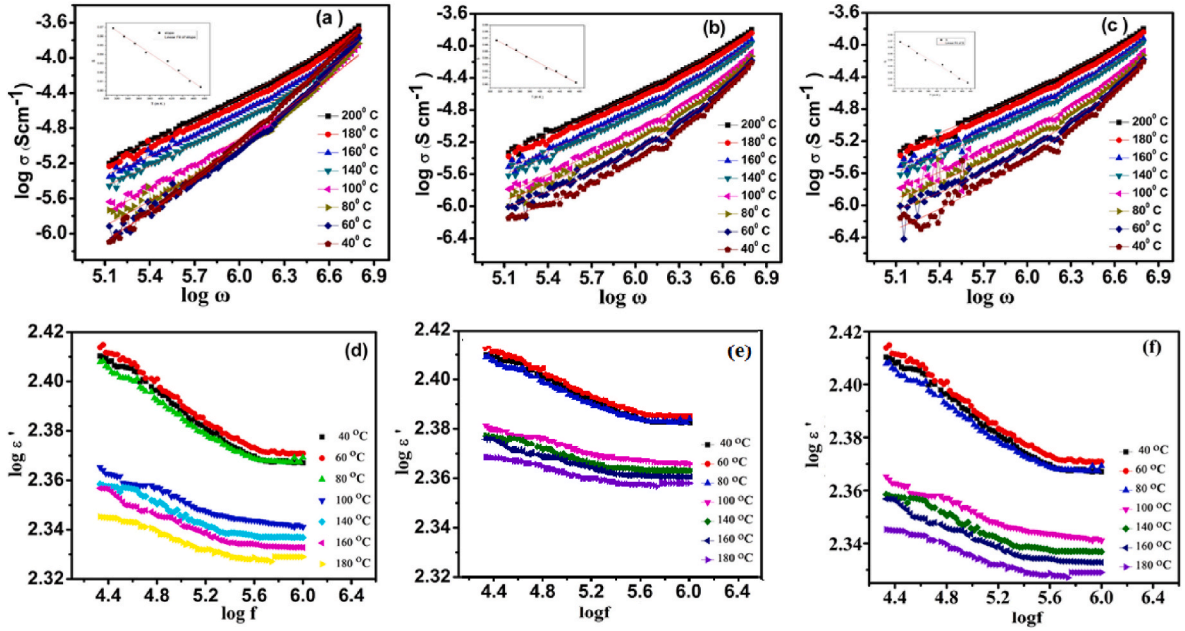

Fig. 3. (a–c) Graph of a.c conductivity of 0.2 wt %, 0.6 wt% and 1.0 wt% Fe doped MgO nanoparticle respectively. Fig. 3(d–f)Graph of dielectric constant vs. Frequency of 0.2 wt %, 0.6 wt% and 1.0 wt% Fe doped MgO nanoparticle respectively.

dispersion with concentrations ranging from 0 to 6.5 µg/ml were mixed to agar cups. Subsequently, the Petri dishes were placed in an incubator at 37 °C overnight, and the diameter of the inhibition zones around each cup was measured at each concentration. To evaluate the MIC of the nanoparticles, the live count technique was employed. 2 ml of nutrient broth with an equal amount of bacterial inoculums with different concentrations of Fe doped MgO nanoparticles were used for this purpose. Following a 48-h incubation period, the viable bacteria within each

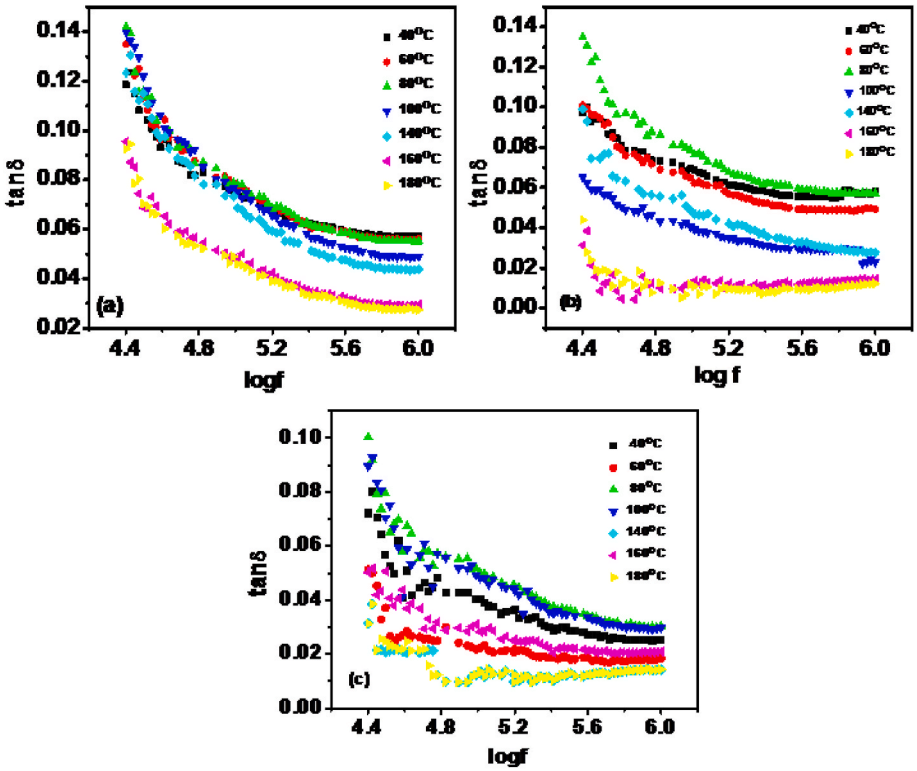

Fig. 4. (a–c) Graph of Loss vs. Frequency at the concentration of 0.2 wt %, 0.6 wt% and 1.0 wt% Fe doped MgO nanoparticle respectively.

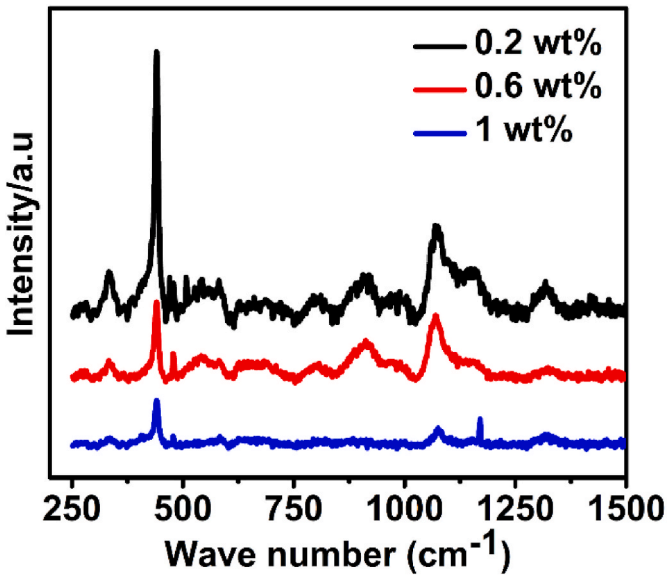

Fig. 5. Graph of Raman Spectra at different concentration of 0.2 wt %, 0.6 wt% and 1.0 wt% Fe doped MgO nanoparticle respectively.

culture were encouraged to proliferate by transferring them onto nutrient-filled agar plates. These agar plates were then subjected to additional 48-h incubation at 37 °C, at which point the colony count was ascertained.

3. Results and discussion

3.1. Microstructural characterization

In Fig. 1, the X-ray diffraction pattern for Fe-doped MgO nanomaterials at various concentrations of Fe (0.2 wt%, 0.6 wt%, and 1 wt%) is depicted, revealing their crystalline nature with an average crystal size falling within the range of 9 to 7 nm. The crystalline size of the Fe doped MgO nanoparticles are determined by Scherrer method.[23] Crystalline size and lattice parameters are depicted in Table 1. All the major peaks are indexed with standard FCC phase of MgO with JCPDS card no 78–0430 confirmed the crystalline property as well as crystalline structure of the synthesized nanoparticles described elsewhere.[24] Fig. 2 (a–c) depicted the images captured by TEM of experimented nanoparticles. The average dimension of 0.2 wt%, 0.6 wt% and 1 wt% concentration of sample nanoparticle is detected to be 9.12 nm, 7.86 nm and 7.24 nm respectively. Synthesized Fe doped MgO nanoparticles seem to be cubical shape and regular crystal structures without any perceptible pores. Fig. 2(d) exhibits the SAD pattern with some clear diffraction points of different concentration of sample. In Fig. 3(a–c), it is evident that as the frequency (f) decreases at a constant temperature, the dielectric permittivity exhibits a progressive increase for varying concentrations of experimental nanoparticles. In the lower frequency range, a notable surge in the real component of the dielectric constant is observed, signifying the existence of large dispersion in charge diffusion between the two electrodes. Due to the relaxation process, electrical dipoles are frozen, which causes a significant reduction in the low frequency area. As the applied field varies, the polarization decreases and the inhomogeneous characteristics of the material hinder the charge carriers in the conducting zone.

The total ac conductivity of the experimental sample has been studied within the frequency range from 20Hz to 1 MHz when the temperature ranges from 273K to 523K. From the observed data, it can be shown that conductivity at higher frequency regions increases as frequency increases, whereas conductivity at lower frequency regions is practically frequency-independent. Total conductivity can be expressed as the following using Jonscher's power law variation.[25,26]

$$\sigma'(f) = \sigma_{dc} + \sigma_{ac}(f) = \sigma_{dc} + \gamma f^{n} \quad (2)$$

where $0< n <1$ Here σ_{dc}, γ and n are the dc conductivity, temperature-

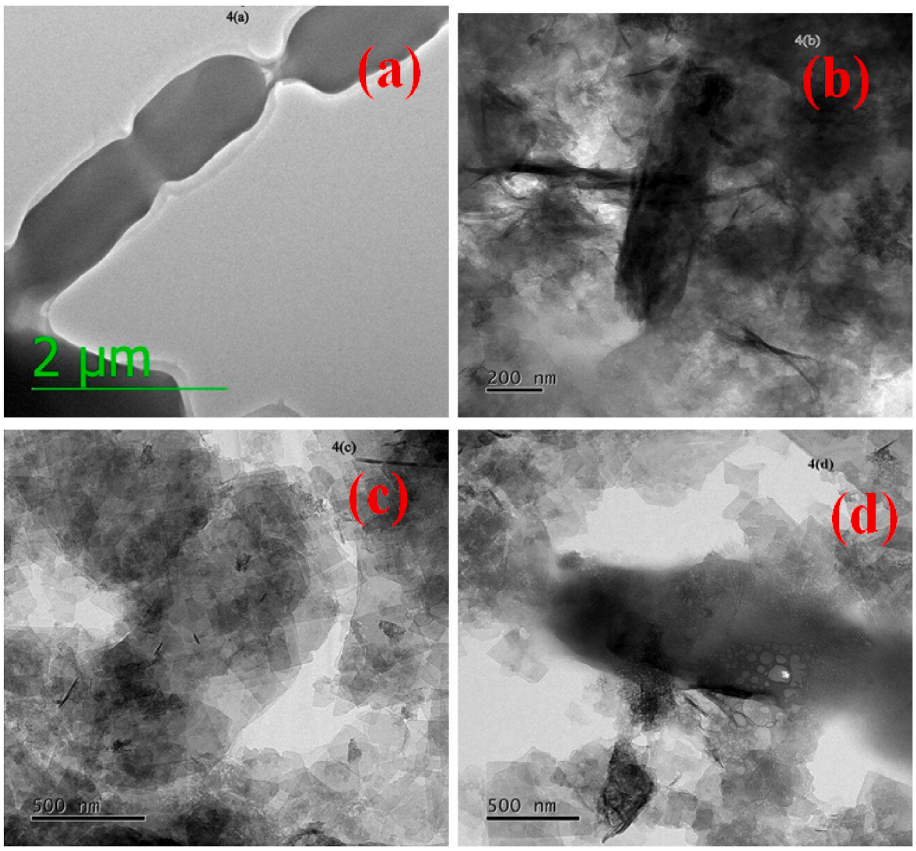

Fig. 6. (a) Images captured by TEM of cell morphology of untreated *E.coli*. Fig. 6(b–d) Images captured by TEM for the cell morphology of *E.coli* after the treatment with 0.2 wt %, 0.6 wt% and 1.0 wt% Fe doped MgO nanoparticle respectively.

dependent constant, and power-law exponent ($n \leq 1$). The variation in total conductivity with different temperatures and frequencies for different doped samples can be seen in Fig. 3(d–f). We can calculate the values of σ_{dc} and n at different temperatures by fitting equation (2). The "n" is temperature independent for the Quantum Mechanical Tunnelling model (QMT).[27] But for the non-overlapping small polaron tunnelling (NSPT) model "n" increases with the increasing temperature.[28] Different values of exponent "n" might result from strong electron-phonon interactions and a small conduction band.[29] Sometimes, "n" decreases initially and then increase as the temperature rises, which is described by the model of overlapping large polaron tunneling.[30] The Correlated Barrier Hopping model (CBH)[31] is also significant in explaining the conduction process, as it explains the hopping of charges over the barrier and it is also significant to explain the conduction process. Frequency exponent "n" can be represented by

$$n = 1 - \frac{6k_BT}{\left[W_H - k_BTln\left(\frac{1}{\omega\tau_0}\right)\right]}$$

The parameters τ_0 and W_H shows the respective values of relaxation time and barrier height respectively. The frequency exponent variation "n" is independent of frequency when value of the parameter, $\frac{W_H}{K_BT}$ is very large.[32] In the figure, theoretical data is shown by point notation and theoretical best fit value is represented by solid line. The fitted value of W_H and τ_0 for 0.2 wt%,0.6 wt% and 1 wt% Fe doped MgO nanoparticles are respectively (1.27 eV and 5.14×10^{-13}s) ; (1.28 eV and 5.11×10^{-13} s); (1.29 eV and 5.12×10^{-13} s). To assess the charge storage potential of Fe-doped MgO nanoparticles across different Fe concentrations (0.2 wt%, 0.6 wt%, and 1.0 wt%), it is important to study the loss factor. This crucial factor, indicative of the balance between capacitive and resistive energy. Within this framework, the system exhibits dielectric loss factors illustrated in Fig. 4(a–c). The loss arises due to dipolar orientation loss, vibrational loss, DC conduction and interfacial losses at grain boundaries—especially noticeable at low frequencies.[33] The investigation of the Raman spectra of Fe-doped MgO nanoparticles, covered the frequency range of 250–1500 cm^{-1}, shown in Fig. 5.

3.2. Antibacterial characterization

Fig. 6(a) displays the TEM image of the untreated *E.coli* cell structure, devoid of any Fe-doped MgO nanoparticle treatment. Conversely, Fig. 6 (b–d) shows TEM images of *E.coli* following exposure to Fe-doped MgO nanoparticles at concentrations of 0.2 wt%, 0.6 wt%, and 1 wt%, respectively. Similarly, Fig. 7 exhibit cell structure for the *Bacillus* sp. captured by the TEM untreated with Fe doped MgO nanoparticles and after treatment with 0.2 wt%, 0.6 wt% and 1 wt% above mentioned nanoparticles. It is observed that the treatment with different concentrations of Fe doped MgO nanoparticles leads towards a significant cell wall disintegration of the pathogen strain. The treatment results in distinct morphological changes in both pathogens, altering their overall shape in comparison to the untreated samples. According to the agar-cup method, the cup size of for both microbes treated with the 0.2 wt%, 0.6 wt%, and 1 wt% Fe doped MgO nanoparticles remains unchanged up to a concentration of 2.5 μg/ml. The antibacterial effect of the nanoparticles is considerably pronounced in *Bacillus* sp. than *E.coli* as demonstrated by the different size of zones in the medium, as shown in Table 2.The MIC levels of experimented pathogens are illustrated in Fig. 8(a–c) and Fig. 9(a–c) respectively.MIC levels are consistent with agar-cup method. The ½ MIC for *Bacillus* sp. is 1.75 μg/ml, while that for *E.coli* is 2.75 μg/ml, indicating that *Bacillus* sp. is more sensitive to the bactericidal effect of Fe doped MgO nanoparticles than *E.coli*. Fig. 10

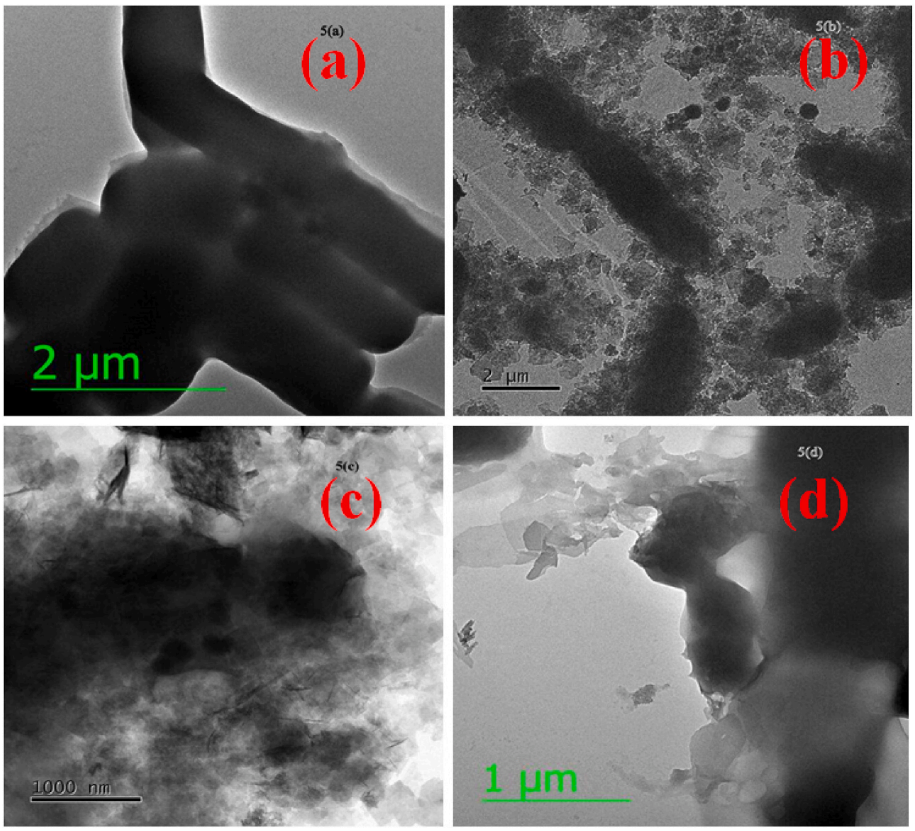

Fig. 7. (a) Images captured by TEM of cell morphology of untreated *Bacillus* sp.Fig. 7(b–d) Images captured by TEM for the cell morphology of *Bacillus* sp. after the treatment with 0.2 wt %, 0.6 wt% and 1.0 wt% Fe doped MgO nanoparticle respectively.

Table 2
Zone diameter measured in Agar Cup method: Inclusive bore diameter 9 mm.

Name of pathogens↓	Diameter of inhabitation zone						
	Concentration of samples ↓(in µg/ml)						
	0	1.5	2.5	3.5	4.5	5.5	6.5
	Diameter of inhabitation zone↓(in mm)						
E.Coli (treated with 0.2 % Fe doped MgO nanoparticle)	*9*			*14.5*	*16*	*17*	*18*
E.Coli (treated with 0.6 % Fe doped MgO nanoparticle)				*15*	*16.5*	*17.5*	*19*
E.Coli (treated with 1 % Fe doped MgO nanoparticle)				*15.5*	*17*	*19*	*19.5*
E.Coli (treated with 1.2 % Fe doped MgO nanoparticle)				*15.5*	*17.5*	*19*	*19.5*
E.Coli (treated with 1.5 % Fe doped MgO nanoparticle)				*15.5*	*17.5*	*19*	*19.5*
Name of pathogens↓	*Concentration of samples ↓(in µg/ml)*						
	0	*1.5*	*2.5*	*3.5*	*4.5*	*5.5*	*6.5*
	Diameter of inhabitation zone↓(in mm)						
Bacillus sp. (treated with 0.2 % Fe doped MgO nanoparticle)	*9*			*15.5*	*16.5*	*17.5*	*18.5*
Bacillus sp. (treated with 0.6 % Fe doped MgO nanoparticle)				*16*	*16.5*	*17.5*	*19*
Bacillus sp. (treated with 1 % Fe doped MgO nanoparticle)				*16.5*	*17*	*18*	*19.5*
Bacillus sp. (treated with 1 % Fe doped MgO nanoparticle)				*16.5*	*17*	*18*	*19.5*
Bacillus sp. (treated with 1 % Fe doped MgO nanoparticle)				*16.5*	*17*	*18*	*19.5*

(a–d) display the log normal distribution of particle numbers with particle size (inside and outside the cell) for *Bacillus* sp. and *E.coli* which is treated with Fe doped MgO nanoparticles. It is observed that the particle sizes inside and outside the cells for both microbes are nearly identical before and after treatment with experimented nanoparticles.

4. Discussion

The TEM analyses reveal a crucial aspect in our research, highlighting the penetration of Fe-doped MgO nanoparticles into microbial cells, along with their impact on the cell walls. The observed antibacterial effect can be attributed to the chemical properties of these nanoparticles. This present study reveals that antibacterial activity which is guided by the release of toxicity from ions of metals and simultaneously producing of intracellular reactive oxygen species (ROS) upon microbial. The ferromagnetic property of Fe doped MgO nanoparticle has also enormous significance towards antibacterial activity.[34]The ferromagnetism in Fe doped MgO nanoparticle is responsible for generation of more oxygen vacancies at the surface of nanocrystal.[35–37] Several peaks with different intensities were detected, with the most prominent ones being at around 440 cm^{-1} and 1070 cm^{-1}.The intensity and full width at half maximum (FWHM) of the Raman spectra play a crucial role in assessing the order of materials.A decrease in the intensity of Raman peaks signifies an increase in the level of disorder, such as the presence of vacancies or defects on the surface of the material. During our experiment, we observed a substantial decrease in the magnitude of all peaks as the concentration of Fe doping rose in the MgO samples.As a result, the disorder on the surface, which is characterized by oxygen defects and vacancies, increased as the Fe doping concentrations became higher. The MgO nanoparticles, when doped with Fe at concentrations of 1 wt% and 0.6 wt%, showed less intense Raman signals instead of 0.2 wt%, suggesting a higher occurrence of surface defects such as oxygen

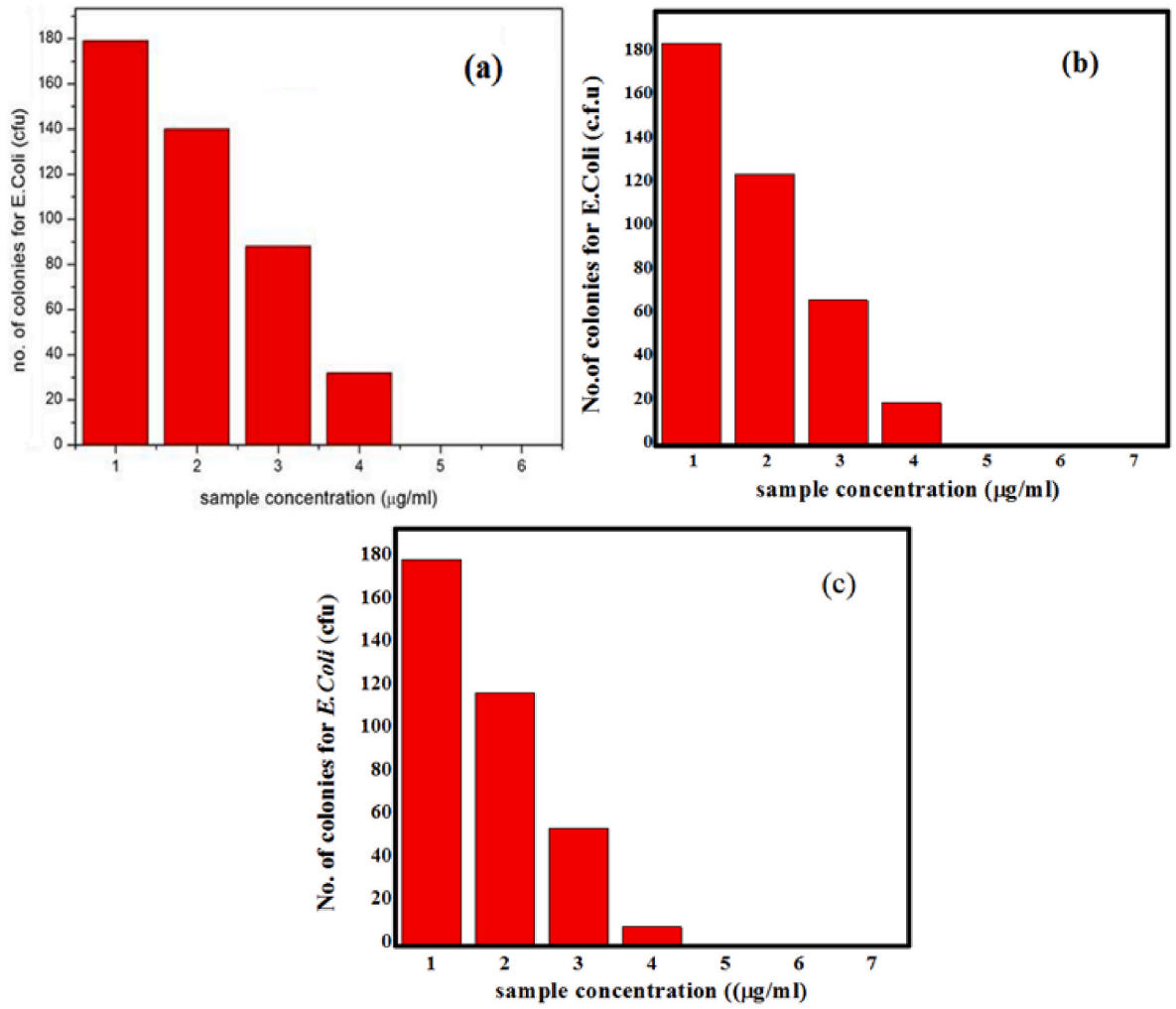

Fig. 8. (a–c) Colony count plotting for *E.coli sp.* for 0.2 wt %, 0.6 wt% and 1.0 wt% Fe doped MgO nanoparticles to calculate MIC respectively.

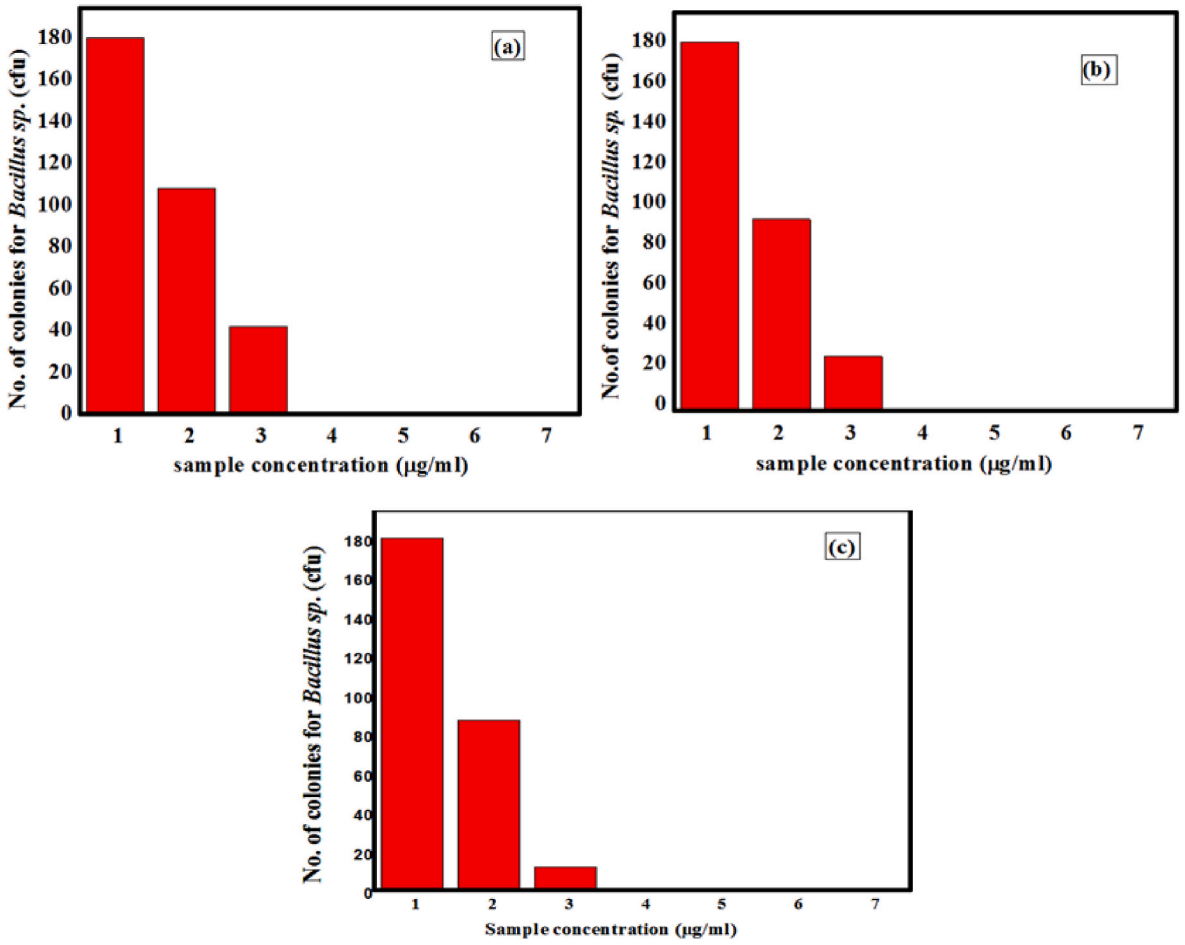

Fig. 9. (a–c) Colony count plotting *Bacillus* sp. for of 0.2 wt %, 0.6 wt% and 1.0 wt% Fe doped MgO nanoparticles to calculate MIC respectively.

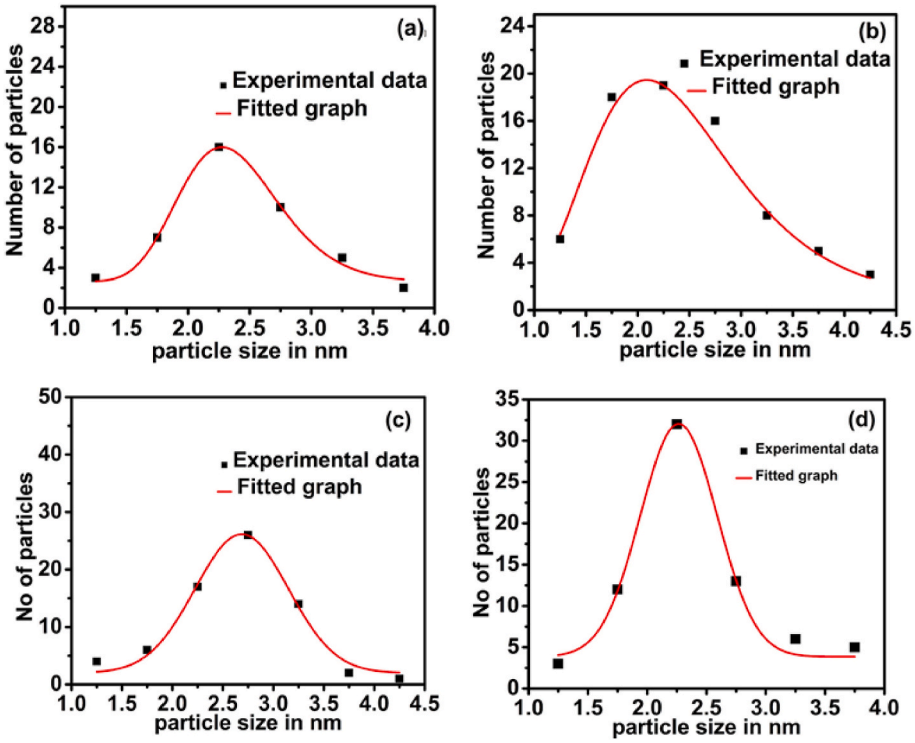

Fig. 10. (a–b) log normal distribution plot of number of particles inside and outside cell of *Bacillus* sp. treated with Fe doped MgO nanoparticles respectively. Fig. 10 (c-d)Plot of log normal distribution of number of particles inside and outside cell of *E.coli* treated with Fe doped MgO nanoparticle.

vacancies.This observation aligns with almost similar explanation provided by Selim et al. in their Raman spectroscopy study on MgO nanoparticles.[38] The generated oxygen vacancies are absorbed on the Bacterial cell's exterior.[39] The capacity of a substance to disrupt the bacterial cell wall, altering its permeability and hindering its ability to carry out essential respiratory functions, ultimately leads to the demise of the cell.[36,40] The sensitivity of superoxide radicals is notable. They cause an impact by disrupting the peptide cross-linkages carbonyl group of the cell wall. In our study, we've observed that gram-positive bacteria exhibit higher antibacterial activity when compared to gram-negative bacteria, primarily attributed to the additional barrier in their membrane, which hinders the easy diffusion of superoxide radicals. Another crucial factor influencing the effectiveness of the experimental nanoparticles in demonstrating strong antibacterial activity is their particle size. Moreover, bacterial cell death can be linked to its structure, size, and surface properties. From different studies it has been demonstrated that smaller particles with larger surface areas display enhanced antibacterial activity when contrasted with larger nanoparticles, due to presence of higher number of reactive groups.[41,42] The shape of bacterial cells is regulated by various proteins, including FtsZ, MerB, and crescentin. The MreB protein plays a crucial role in cell wall regeneration. The shape of *E.coli* cells can transform from rod shape to spherical shape due to depolymerisation of this proteins.[37] The ½ MIC for *E.coli* is seemed to be 2.75 μg/ml where as for *Bacillus* sp. is 1.75 μg/ml when the microbials are treated with Fe doped MgO nanoparticles. But we can find that the use of MgO nanoparticles shows the ½ MIC for *E.coli* is 3.75 μg/ml and for *Bacillus* sp. is 3.0 μg/ml.[37] Therefore, Fe doped MgO exhibits more antibacterial activity instead of MgO nanoparticles towards the bacterial pathogens.

5. Conclusion

Our finding reveals that Fe doped MgO nanoparticles demonstrate significantly higher antibacterial efficiency when compared to their MgO nanoparticles. A lower concentration is needed to observe the antibacterial effects of Fe doped MgO nanoparticles compared to MgO nanoparticles. From the study of electrical properties of experimental nanoparticles it has been observed that the dielectric permittivity of the sample increases as the frequency decreases and the value of frequency dependent constant (s) decreases as the temperature increases.

Declaration of competing interest

The authors declare that they have no known competing financial interests or personal relationships that could have appeared to influence the work reported in this paper.

Acknowledgements

This work was partially supported by Centre of Excellence at the National Institute of Technology, Durgapur. The laboratory facility also provided by the Botany Department of B.B.College, Asansol. The authors would like to acknowledge their principal assistance.

References

1. Bharti SP, Singh E, Kumar U. *Nanosci. Nanotech. Res.* 2017;4:115–119. https://doi.org/10.12691/nnr-4-3-5.
2. Raveendra RS, Prashanth PA, Daruka Prasad B, et al. *Int J Sci Res.* 2013;1.
3. Soares Jr FH, Pinheiro AVB, Morales MA, Soares JM. *Mater Lett.* 2013;113:67–70. https://doi.org/10.1016/j.matlet.2013.09.057.
4. Genchi GG, Marino A, Tapeinos C, Ciofani G. *Front Bioeng Biotechnol.* 2017;5:80. https://doi.org/10.3389/fbioe.2017.00080.
5. Patra JK, Das G, Fraceto LF, et al. *J Nanobiotechnol.* 2018;16:1–33. https://doi.org/10.1186/s12951-018-0392-8.
6. Huh AJ, Kwon YJ. *J Contr Release.* 2011;156:128–145. https://doi.org/10.1016/j.jconrel.2011.07.002.
7. Lee NY, Ko WC, Hsueh PR. *Front Pharmacol.* 2019;10:1153. https://doi.org/10.3389/fphar.2019.01153.
8. Aghebati-Maleki A, Dolati S, Ahmadi M, et al. *J Cell Physiol.* 2020;235:1962–1972. https://doi.org/10.1002/jcp.29126.
9. Nune SK, Gunda P, Thallapally PK, Lin YY, Laird Forrest M, Berkland CJ. *Expet Opin Drug Deliv.* 2009;6:1175–1194. https://doi.org/10.1517/17425240903229031.
10. Wolfbeis OS. *Chem Soc Rev.* 2015;44:4743–4768. https://doi.org/10.1039/c4cs00392f.

11. Boschi F, De Sanctis F. *Eur J Histochem: EJH*. 2017;61:2830. https://doi.org/10.4081/ejh.2017.2830.
12. Varna M, Xouan HV, Fort E. *WIREs Nanomed Nanobiotechnol*. 2018;10:1470. https://doi.org/10.1002/wnan.1470.
13. Kumar VV, Anthony SP. *Surf Chem Nanobiomat*. 2016;3:265–300. https://doi.org/10.1016/B978-0-323-42861-3.00009-1.
14. Karthik K, Dhanuskodi S, Gobinath C, Prabukumar S, Sivaramakrishnan S. *J Photochem Photobiol B Biol*. 2019;190:8–20. https://doi.org/10.1016/j.jphotobiol.2018.11.001.
15. He X, Deng H, Hwang HM. *J Food Drug Anal*. 2019;27:1–21. https://doi.org/10.1016/j.jfda.2018.12.002.
16. Laurenti M, Cauda V. *Coatings*. 2018;8:67. https://doi.org/10.3390/coatings8020067.
17. Znaidi L. *Mater Sci Eng, B*. 2010;174:18–30. https://doi.org/10.1016/j.mseb.2010.07.001.
18. Bagga S, Akhtar J, Mishra S. *AIP Conf Proc*. 2018;1989, 020004. https://doi.org/10.1063/1.5047680.
19. Cauda V, Pugliese D, Garino N, et al. *Energy*. 2014;65:639–646. https://doi.org/10.1016/j.energy.2013.12.025.
20. Yi GC, Wang C, Park WI. *Semicond Sci Technol*. 2005;20:22. https://doi.org/10.1088/0268-1242/20/4/003.
21. Li YB, Bando Y, Sato T, Kurashima K. *Appl Phys Lett*. 2002;81:144–146. https://doi.org/10.1063/1.1492008.
22. Garino N, Limongi T, Dumontel B, et al. *Nanomaterials*. 2019;9:212. https://doi.org/10.3390/nano9020212.
23. Saadi Hajer, Benzarti Zohra, Pedro Sanguino, Pina João, Abdelmoula Najmeddine, Seixas de Melo João Sergio. *J Mater Sci Mater Electron*. 2023;34:116. https://doi.org/10.1007/s10854-022-09470-5.
24. Phokha S, Klinkaewnarong J, Hunpratub S, Boonserm K, Swatsitang E, Maensiri S. *J Mater Sci Mater Electron*. 2016;27:33–39. https://doi.org/10.1007/s10854-015-3713-9.
25. Long AR. *Adv Phys*. 1982;31:553–637. https://doi.org/10.1080/00018738200101418.
26. Hu Y, Chen C, Wen Y, et al. *Compos Sci Technol*. 2021;209, 108760. https://doi.org/10.1016/j.compscitech.2021.108760.
27. Pollak M. *Phil Mag*. 2011;23:519–542. https://doi.org/10.1080/14786437108216402.
28. Ghosh A. *Phys Rev B*. 1990;42:5665.
29. Durán A, Verdin E, Escamilla R, Morales F, Escudero R. *Mater Chem Phys*. 2012;133:1011–1017. https://doi.org/10.1016/j.matchemphys.2012.02.008.
30. Long AR. *Adv Phys*. 1982;31:553–637. https://doi.org/10.1080/00018738200101418.
31. Elliott SR. *Adv Phys*. 1987;36:135–217. https://doi.org/10.1080/00018738700101971.
32. Ghosh M, Barman A, De SK, Chatterjee S. *J Appl Phys*. 1998;84:806–811. https://doi.org/10.1063/1.368141.
33. Jan T, Ahmad Rizvi M, Moosvi SK, Najar MH, Husain Mir S, Peerzada GM. *ACS*. 2022;6(11):7413–7421. https://doi.org/10.1021/acsomega.0c05799.
34. Paramanantham P, Antony AP, Lal SS, et al. *Scientific African*. 2018;1, 00007. https://doi.org/10.1016/j.sciaf.2018.e00007.
35. Yi N, Ma Y, Wang Z, et al. *J Rare Earths*. 2022. https://doi.org/10.1016/j.jre.2022.09.016.
36. Yun H, Kim J, Paik T, et al. *J Appl Phys*. 2016;119, 113901. https://doi.org/10.1063/1.4942865.
37. Choudhury B, Choudhury A. *Mater Res Express*. 2014;1, 025026. https://doi.org/10.1088/2053-1591/1/2/025026.
38. Demirci S, Yildirim BK, Tünçay MM, et al. *J Sol Gel Sci Technol*. 2021;99:576–588. https://doi.org/10.1007/s10971-021-05609-8.
39. Maji J, Pandey S, Basu S. *Bull Mater Sci*. 2020;43:1–10. https://doi.org/10.1007/s12034-019-1963-5.
40. Ramanujam K, Sundrarajan M. *J Photochem Photobiol B Biol*. 2014;141:296–300. https://doi.org/10.1016/j.jphotobiol.2014.09.011.
41. Leung YH, Ng AM, Xu X, et al. *Small*. 2014;10:1171–1183. https://doi.org/10.1002/smll.201302434.
42. Raghupathi KR, Koodali RT, Manna AC. *Langmuir*. 2011;27(7):4020–4028. https://doi.org/10.1021/la104825u.